



New generation of satellite-derived ocean thermal structure for the western north pacific typhoon intensity forecasting



Iam-Fei Pun^{a,b}, I.-I. Lin^{a,c,*}, Dong S. Ko^d

^a Department of Atmospheric Sciences, National Taiwan University, Taipei, Taiwan

^b Woods Hole Oceanographic Institution, Woods Hole, MA, USA

^c Research Center for Environmental Changes, Academia Sinica, Taipei, Taiwan

^d Naval Research Laboratory, Stennis Space Center, MS, USA

ARTICLE INFO

Article history:

Available online 26 October 2013

ABSTRACT

Ocean thermal structure is critical for the intensity change of tropical cyclones (TCs). It has been operationally derived from satellite altimetry for TC forecasting and research. The existing derivation is, however, based on a simple two-layer method; as a result, only two isotherms can be obtained to coarsely characterize the subsurface ocean thermal structure. Improvement on the vertical resolution to enhance ocean characterization is desirable for more accurately estimating ocean's energy supply for TC intensity change.

In this study, we present a new generation of derivation to improve ocean's subsurface characterization for the Western North Pacific Ocean (WNPO) because this region has the highest TC occurrence on the Earth. In addition to the presently used two isotherms for the depths of 20 °C and 26 °C isotherms (D20 and D26), we derive continuous isotherms from D4 up to D29 (maximum 26 subsurface layers) to characterize the subsurface ocean thermal structure in detail. This is achieved through applying a large set (>38,000) of *in situ* Argo thermal profiles to regression development. A smaller set of *in situ* Argo profiles (>7000), independent of those used for regression, is utilized for validation, to assess the accuracy of the new derivation. The root-mean-square differences (RMSDs) between the derived and the *in situ* isotherms are found to be within ~10–20 m for the upper isotherms (D20 to D29) and within ~40–60 m for the lower isotherms (D4 to D19). No significant biases of derived isotherms are found.

In addition to increasing the vertical resolution from two layers to 26 layers, higher accuracy for the two isotherms of D20 and D26 is also achieved. For example, in the existing two-layer method, D20 in the northern WNPO is grossly overestimated with a high RMSD of ~80–100 m; the new method significantly reduces the RMSD to ~20 m. Better subsurface characterization leads to improvement in important TC-intensity related parameters, like during-cyclone sea surface temperature (SST) cooling and air-sea enthalpy flux supply. Based on a series of ocean mixed layer numerical experiments using 16 randomly-selected profiles, we find that the error in SST cooling (air-sea flux supply) can be reduced from 36% (120%) to 13% (20%).

© 2013 Elsevier Ltd. All rights reserved.

1. Introduction

Ocean thermal structure (OTS) plays a critical role in the intensity change of tropical cyclones (TCs), due to the energy supply from the ocean to the TC (Leipper and Volgenau, 1972; Gray, 1979; Holliday and Thompson, 1979; Emanuel, 1999; Schade and Emanuel, 1999; Shay et al., 2000; Goni and Trinanes, 2003; Lin et al., 2005, 2008, 2013; Wu et al., 2007; Goni et al., 2009; Shay and Brewster, 2010; Balaguru et al., 2012; Moon and Kwon, 2012; Cione et al., 2013). From the perspective of TC, OTS typically

concerns temperatures in the top 200–300 m, because the interaction between TC and the ocean takes place within this layer. When a TC passes over the ocean, the underlying OTS is disturbed and mixed by the intense wind associated with the TC. As a result, the relatively cold water from deeper ocean is entrained and/or upwelled into the surface layer, producing the renowned TC-induced sea surface temperature (SST) cooling (Chang and Anthes, 1978; Price, 1981; Bender and Ginis, 2000; Cione and Uhlhorn, 2003; Lin et al., 2003a,b; Tseng et al., 2010). This SST cooling can significantly reduce the enthalpy (i.e., sensible heat + latent heat) flux supply from the ocean to the TC; thus it is an important negative feedback mechanism for TC intensification (Gallacher et al., 1989; Bender et al., 1993; Emanuel, 1999; Schade and Emanuel, 1999; Bender and Ginis, 2000; Hong et al., 2000; Cione and Uhlhorn, 2003; Emanuel et al., 2004; Lin et al., 2008, 2009a,

* Corresponding author at: Department of Atmospheric Sciences, National Taiwan University, No. 1, Sec. 4, Roosevelt Rd., Taipei 106, Taiwan. Tel.: +886 2 33663917.

E-mail address: iilin@as.ntu.edu.tw (I.-I. Lin).

2013; Balaguru et al., 2012; Moon and Kwon, 2012). Over a thicker (thinner) and warmer (colder) OTS region, the SST cooling is generally suppressed (enhanced) (Price, 1981; Shay et al., 2000; Lin et al., 2009b, 2013; Goni et al., 2009); thus, the OTS is a critical parameter in TC intensity forecasting and research.

To obtain synoptic OTS observations operationally over the global TC basins, *in situ* observations are clearly not the solution. The launch of satellite altimeters in the 1990s has enabled operational derivation of OTS using altimetry sea surface height anomaly (SSHA) observations (Goni et al., 1996, 2009; Shay et al., 2000; Willis et al., 2003; Pun et al., 2007, 2011; Shay and Brewster, 2010). These satellite-derived OTS fields have made significant contributions to our understanding of the interaction between TCs and the ocean (Shay et al., 2000; Goni and Trinanes, 2003; Lin et al., 2005, 2008; Pun et al., 2007; Mainelli et al., 2008; Goni et al., 2009; Shay and Brewster, 2010). The existing derivation is mainly based on a two-layer reduced gravity model (hereafter referred to as “TLM”) where only two isotherms (i.e., the depths of 20 °C and

26 °C isotherms, or D20 and D26) are derived to coarsely characterize the OTS (Shay et al., 2000; Goni and Trinanes, 2003; Pun et al., 2007; Goni et al., 2009; Shay and Brewster, 2010). The TLM has been used extensively and has much contributed to understanding the role ocean’s subsurface thermal structure (e.g., the role of warm ocean eddies) plays in tropical cyclone’s intensity change (Shay et al., 2000; Goni and Trinanes, 2003; Mainelli et al., 2008; Goni et al., 2009; Lin et al., 2009b; Shay and Brewster, 2010; Pun et al., 2011) and to monitoring long-term subsurface changes in typhoon developing region (Pun et al., 2013). However, improvement on vertical resolution of satellite-derived OTS to enhance ocean characterization is desirable. This series of work is dedicated to this goal. We aim to develop a new generation of derivation to improve ocean’s subsurface characterization over global TC basins for better TC intensity forecasting and research. Since the Western North Pacific Ocean (WNPO) has the most TCs (i.e., typhoons) on the Earth, the first paper of this series (this study) covers the WNPO.

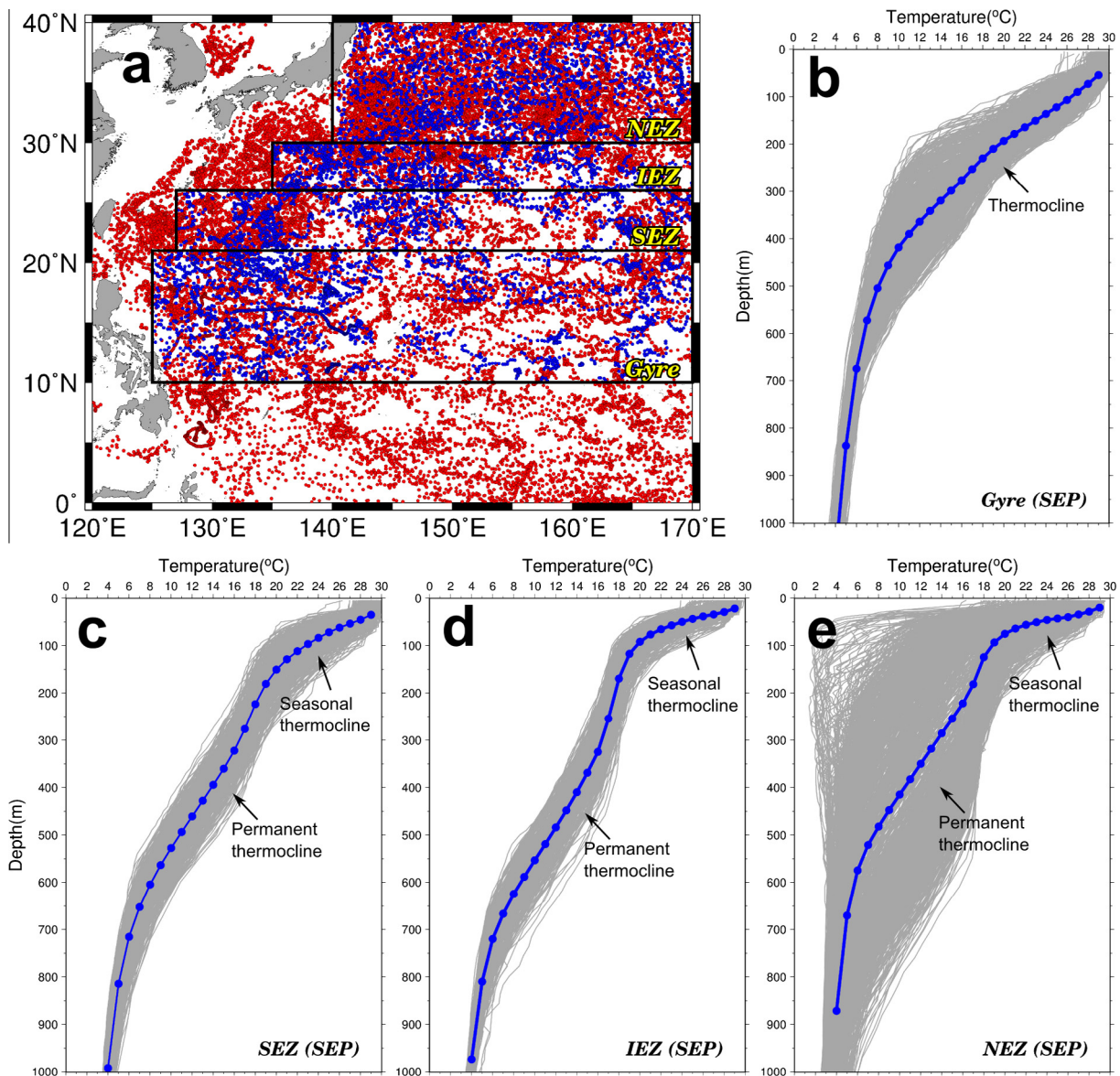


Fig. 1. (a) Locations of Argo profiles used in the present study. Red dots depict 38,556 profiles collected from 2000–2008, and blue dots depict 7036 profiles from 2009–2010. Only typhoon season, May–October, is considered. Four hydrographic zones are indicated. (b–e) Depth–temperature plots of all the Argo profiles (grey curves) in September of 2000–2008 in the Gyre, SEZ, IEZ and NEZ. In (b–e), the blue curves depict the mean profiles and the blue dots depict the mean depths of isotherms from D29 to D4. The seasonal and permanent thermoclines are also indicated. (For interpretation of the references to color in this figure legend, the reader is referred to the web version of this article.)

Table 1
Additional quality control for Argo profiles.

Items	Threshold
Problematic floats	WMO ^a instrument type 852
1st Points of temperature	<0 °C or >35 °C
Temperature jump	>1 °C
Maximum depth	<200 m
Depth jump	>300 m
Valid points	<10 points

^a WMO: World Meteorological Organization.

Fig. 1a depicts the WNPO domain (120–170°E and 0–40°N). According to Lin et al. (2005, 2008) and Pun et al. (2007), four zones with distinctive TC-related OTS characteristics can be found in the WNPO. These zones are the Gyre, Southern Eddy-rich Zone (SEZ), Intermediate Eddy Zone (IEZ), and Northern Eddy-rich Zone (NEZ). The Gyre (125–170°E and 10–21°N) is the region to the south where the deepest and warmest OTS is located. In the SEZ (127–170°E and 21–26°N) and NEZ (140–170°E and 30–40°N), warm and cold ocean eddies frequently appear. Thus, in the SEZ and NEZ, the OTS can greatly fluctuate. Lastly, the IEZ (135–170°E and 26–30°N) is the intermediate region, in between the two eddy-rich zones of SEZ and NEZ (Pun et al., 2007). From the perspective of TC, the OTS shows distinctive differences among these zones (Fig. 1b–e). The Gyre region has the warmest subsurface temperature, as characterized by the deepest D20 and D26. Moving north to the SEZ, IEZ, and NEZ, the OTS shoals significantly poleward. In the NEZ, the OTS is the shallowest and the mean D20 is only around 60 m, much shallower compared to the D20 of ~200 m in the Gyre region. Further details of these four zones and the hydrographical setting of the WNPO can be found in the Supplementary Online Material (SOM).

Pun et al. (2007) assessed the accuracy of the existing TLM derivation in the WNPO. It was found that D20 can be grossly overestimated by more than 100% in the northern WNPO (i.e., the NEZ region). Therefore, in addition to increase the vertical resolution, we intend to find a new method to improve the OTS derivation in the WNPO.

Derivation based on linear regression is an approach which has been used in climate-related studies (Cheney, 1982; Carnes et al., 1990; White and Tai, 1995; Gilson et al., 1998; Willis et al., 2003, 2004) but not in TC-related studies. This is because meaningful linear regressions can only be established with a large number of *in situ* profiles and there was not enough data for TC-related

derivation. To date, with the great enhancement in *in situ* observations from the Argo floats (Gould et al., 2004; Roemmich et al., 2004), it has become possible to apply regression method to derive the OTS for TC-related purposes (Guinehut et al., 2012). In this study, we derive daily, 0.25° OTS from satellite altimetry over the WNPO during the typhoon season (May–October) using a regression method. This is established based on all available (>38,000) *in situ* Argo float profiles collected during the typhoon season in 2000–2008.

2. Data

2.1. Argo profiles

Argo is an autonomous float that continuously measures temperature and salinity profiles in the ocean (typically from surface to 2000 m depth) at a 10-day interval (Gould et al., 2004; Roemmich et al., 2004). Currently, over 3500 Argo floats are collecting data at any given time period, providing an unprecedented number of real-time and high-quality *in situ* measurements over the global oceans. In this study, 11 years of Argo thermal profiles from 2000–2010 are used (Fig. 1a). Profiles in the first nine years of 2000–2008 are used to build the linear regressions between satellite SSHA and subsurface temperature variation, whereas the profiles in the last two years of 2009 and 2010 are used for the validation of the derived OTS.

Although the profiles provided by the Argo data center (www.argo.net) have already gone through a standard quality control (QC) procedure, additional QC is performed to ensure that all the profiles used in this study are in high quality. According to Willis et al. (2009), cold biases were found in some types of Argo floats deployed between mid-2003 and 2006. For this reason, the profiles from the problematic floats are excluded in this study. All of the items and their thresholds for the additional QC are listed in Table 1. On average, about 10% of the profiles were ruled out by this additional QC.

2.2. Satellite SSHA and SST

The near real-time (NRT) daily and delay-time (DT) 7-day merged and gridded SSHA products were employed in this study. Both products have the spatial resolution of 0.25°. They are operationally generated by the Segment Sol multimissions d'Altimétrie, d'Orbitographie et de localisation précise/Data Unification and Altimeter Combination System (SSALTO/DUACS) and distributed

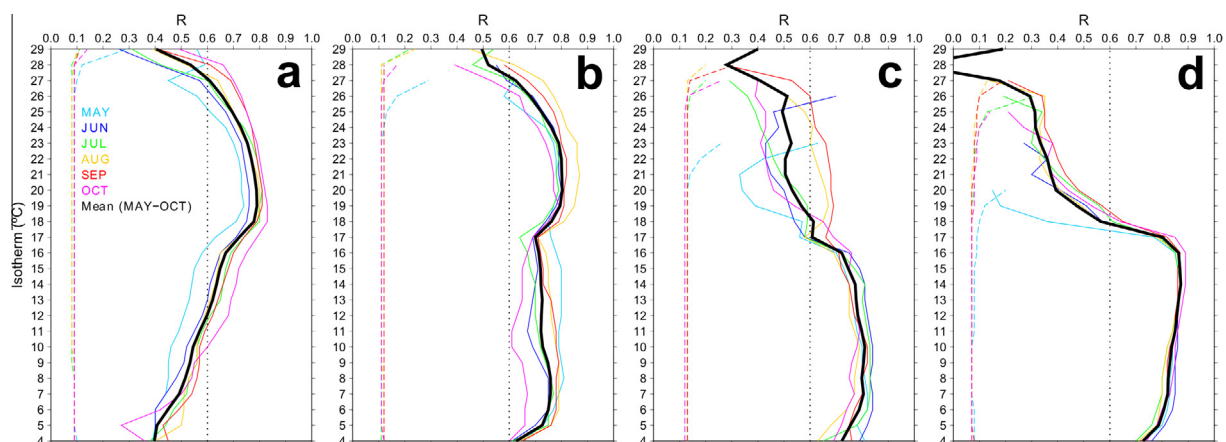


Fig. 2. The monthly correlation (R) between SSHA and the displacements of the isotherms from 29 °C to 4 °C, in (a) the Gyre, (b) the SEZ, (c) the IEZ and (d) the NEZ. The color code for each curve is shown in (a). The dashed lines represent the 99% significance level, and the dotted lines depict $R = 0.6$. (For interpretation of the references to color in this figure legend, the reader is referred to the web version of this article.)

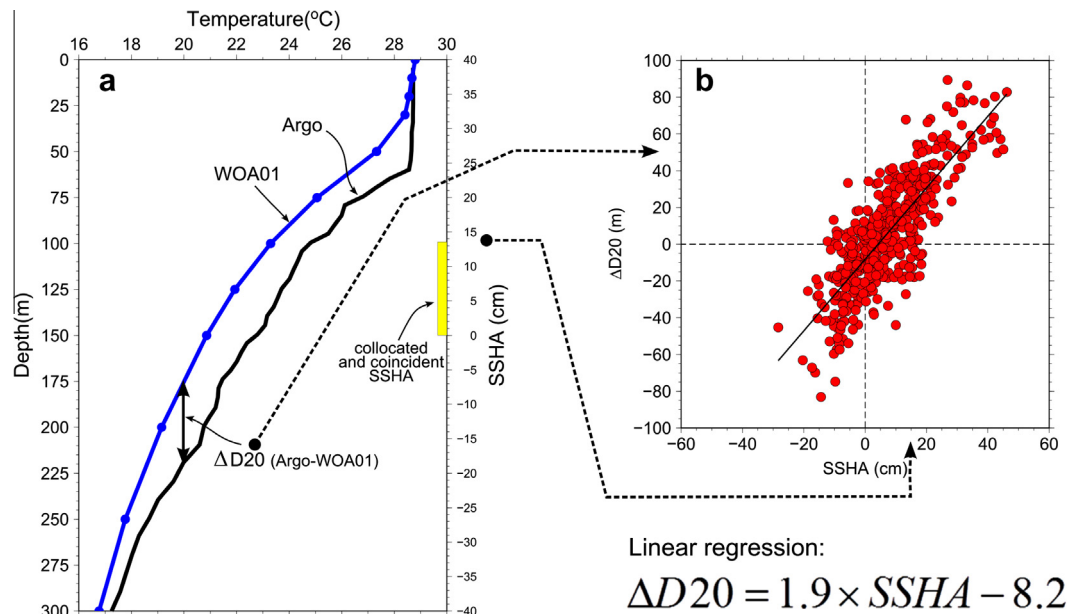


Fig. 3. Schematic diagram shows how a D20 regression is developed. (a) An exemplary depth-temperature profile pair of an Argo *in situ* profile (black) and WOA01 climatological profile (blue). The left axis is depth and the right axis is SSHA. The D20 displacement, i.e. $\Delta D20$, is the difference between the *in situ* and climatology, and its corresponding SSHA value is indicated as a yellow vertical bar. (b) The scatter plot of $\Delta D20$ and SSHA consists of a number of observation pairs. Based on these pairs, a linear regression is developed.

via the Archiving, Validation and Interpretation of Satellite Oceanographic data (AVISO) web site (www.aviso.oceanobs.com). In these products, SSHA measurements from all available altimetry missions are merged to maximize the observations (Ducret et al., 2000; Pascual et al., 2006, 2009). These missions include Ocean Topography Experiment (TOPEX)/Poseidon (T/P), Jason-1, Jason-2, Geosat Follow-On (GFO), Envisat, and European Remote sensing Satellite (ERS) series (Fu et al., 2003; Le Traon and Dibarboure, 2004). This AVISO merged dataset is the most well-known and was widely used in many studies (Niiler et al., 2003; Willis et al., 2004; Qiu and Chen, 2010; Cazenave and Remy, 2011; Chelton et al., 2011). To match the Argo observations, the SSHA data between 2000 and 2010 is used. Initially, the 7-day DT product is used. When the higher temporal-resolution (daily) data from the NRT dataset became available after 5 July 2006, the daily, NRT data is used from 5 July 2006 to 2010.

Besides the SSHA, satellite-observed SST is also used. The version-3 fusion SST is used in this study, which is from the cloud penetrating Tropical Rainfall Measuring Mission/Microwave Imager (TRMM/TMI) and Advanced Microwave Sounding Radiometer for the Earth Observing System (AMSR-E). This dataset is operationally provided by the Remote Sensing Systems with a nominal accuracy of $\sim 0.5^\circ\text{C}$ (Wentz et al., 2000). The spatial and temporal resolutions are 0.25° and daily, respectively.

3. Relationship between SSHA and depth variation of isotherms

Based on the assumption that the change in sea surface height is primarily contributed by the steric effect (i.e., thermal expansion and saline contraction; Gill and Niiler, 1973), the variations in subsurface properties, such as temperature and salinity, are closely related to the variation in SSHA, which is now accurately detected by space-based altimeters. In the tropical and subtropical oceans, the changes in sea surface height are largely dominated by temperature changes in the water column due to thermal expansion (White and Tai, 1995; Gilson et al., 1998; Willis et al., 2003). Thus, positive SSHAs generally reflect subsurface temperatures that are warmer

than the climatology (isotherm deepening below the mean level; Fig. 3a). In contrast, negative SSHAs represent cooler temperatures.

To start, we calculate monthly correlation coefficients between SSHA and the depth variation in each isotherm from D4 to D29 (Fig. 2). The variation of the isotherm depth is the vertical displacement of the *in situ* isotherm (i.e., from Argo) with respect to the monthly climatology field of the World Ocean Atlas 2001 (WOA01; Stephens et al., 2002). In other words, the displacement is the difference between Argo and WOA01 climatology within the same month (Fig. 3a). Thus the correlations in Fig. 2 are based on the observations (i.e., satellite SSHA and Argo temperature profiles from 2000 to 2008). It can be seen that the correlation varies from isotherm to isotherm, from region to region, and from month to month. In the Gyre (Fig. 2a), strong correlation of >0.6 can be found in most isotherms between D12 to D27 with a maximum (~ 0.75) found between D18 and D22. The correlation also varies with month, with slightly lower correlations in May/June and a higher correlation in October. In the SEZ, high correlation of >0.6 is found almost in the entire column of the isotherms (i.e., D4–D27), with a maximum (~ 0.8) found between D19 and D23. Interestingly, a local minimum is found in D17. This may be due to the fact that D17 is located in the transition layer between the seasonal and permanent thermoclines and is expected to be less correlated to SSHA (Fig. 1c).

Moving north, the situation in the IEZ becomes more complex; the isotherms with a higher correlation of >0.6 are generally located below D17 (Fig. 2c), all within the permanent thermocline (Fig. 1d). In contrast, the isotherms above D17 belong to the seasonal thermocline and have lower correlations (temporal maximum correlations are found in August/September). Similar to the SEZ, a local minimum in the IEZ is also found in D17, indicating that the transition layer is also around this isotherm. Finally, in the NEZ (Fig. 2d), the isotherms with the highest correlation (~ 0.8 – 0.9) are found below D17 (i.e., the layer of the permanent thermocline; Fig. 1e).

From above, it can be seen that though SSHA is only used to retrieve D20 and D26 in the current TLM (Shay et al., 2000; Goni and Trinanes, 2003; Pun et al., 2007; Goni et al., 2009; Shay and

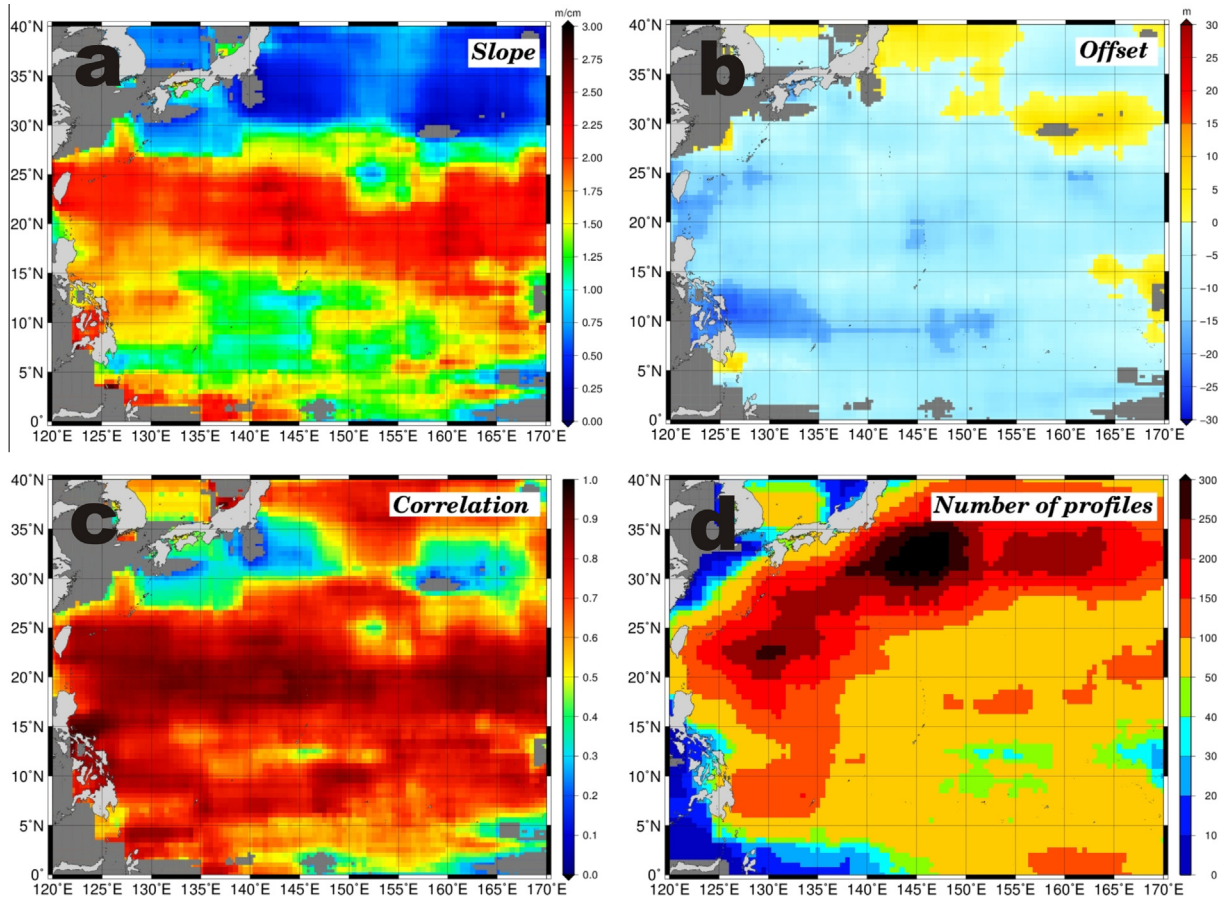


Fig. 4. The spatial distribution of (a) the slope and (b) the offset of the Eq. (2) for D20 in September. (c) The spatial distribution of the correlation between D20 and SSHA. (d) The number of profiles used for developing the regression at each $0.25^\circ \times 0.25^\circ$ grid point. Grey areas represent the significance level <99%.

Brewster, 2010), other isotherms in the WNPO can have similar or even stronger correlations. This suggests that it is possible to retrieve other isotherms using SSHA and not limited to only D20 and D26.

4. Linear regression

A total of 38,556 Argo profiles are used to develop the regressions between SSHA and subsurface isotherm depth variation. We construct a regression at every $0.25^\circ \times 0.25^\circ$ grid and on a monthly basis. The vertical resolution is at 1°C interval from D4 to D29 (26 layers). To have a robust and representative regression, a large number of *in situ* profiles are required. However, in a fine resolution grid of 0.25° , it is unlikely to have a significant number of *in situ* profiles. To solve this problem, we use a moving-window approach. For each grid, profiles within a window of 10° longitude by 5° latitude centered at the grid are binned to calculate the regressions. The reason for using 10° longitude is because there is less variability in the east–west direction (Fig. 1). The regressions are constructed by linearly regressing the isotherm displacements onto their co-incident and co-located SSHA values. The displacement thus is the isotherm depth difference between *in situ* and climatological profiles, representing the deviation from the climatology (Fig. 3a). Here, the climatology field is from the monthly, 0.25° temperature data of the WOA01 (Stephens et al., 2002). The isotherm displacement (ΔD) in each *in situ* profile is derived as:

$$\Delta Di = Di - \bar{Di}, \quad i = 29, 28, \dots, 4, \tag{1}$$

where D and \bar{D} are the *in situ* and climatological depths of isotherm, respectively; and i is the isotherm from 29°C to 4°C .

The displacements in each isotherm of the *in situ* profiles are linearly regressed onto their corresponding SSHA by least square fit (Fig. 3b). The monthly regression equation for each isotherm at each grid is obtained using:

$$\Delta Di = a_{(x,y,m,i)} \times \eta + b_{(x,y,m,i)}, \tag{2}$$

where η is the satellite-observed SSHA; a and b are the linear regression coefficients representing the slope and offset, respectively; both coefficients are a function of location (x,y ; interval of 0.25°), isotherm (i ; D29–D4), and month (m ; May–October). With this set of regression equations, the displacement of an isotherm (ΔDi) can be estimated from the SSHA. The actual depth of the isotherm (Di) is then retrieved by adding the corresponding climatological depth. To precisely demonstrate the derivation of the regression equations (Eq. (2)) from Argo profiles and satellite SSHA, we use D20 as an example to make a schematic diagram (Fig. 3). An Argo profile in Fig. 3a represents one arbitrary point in Fig. 3b. Firstly, $\Delta D20$ is obtained by subtracting the climatological D20 from *in situ* D20, and then paired with co-located and co-incident SSHA (yellow bar in Fig. 3a). Given a large number of $\Delta D20$ -SSHA pairs (red dots in Fig. 3b), a linear regression for D20 is derived. Equations for other isotherms are derived in the same way.

Fig. 4 presents the regression coefficients of Eq. (2) for D20 in September. The regression is developed based on ~ 50 – 300 profiles for each grid (Fig. 4d). One can see that the slope (a) of the regressions exhibits spatial variability. The steepest slope is found near 15 – 25°N , about 2.5 m cm^{-1} , meaning that 1 cm of SSHA can

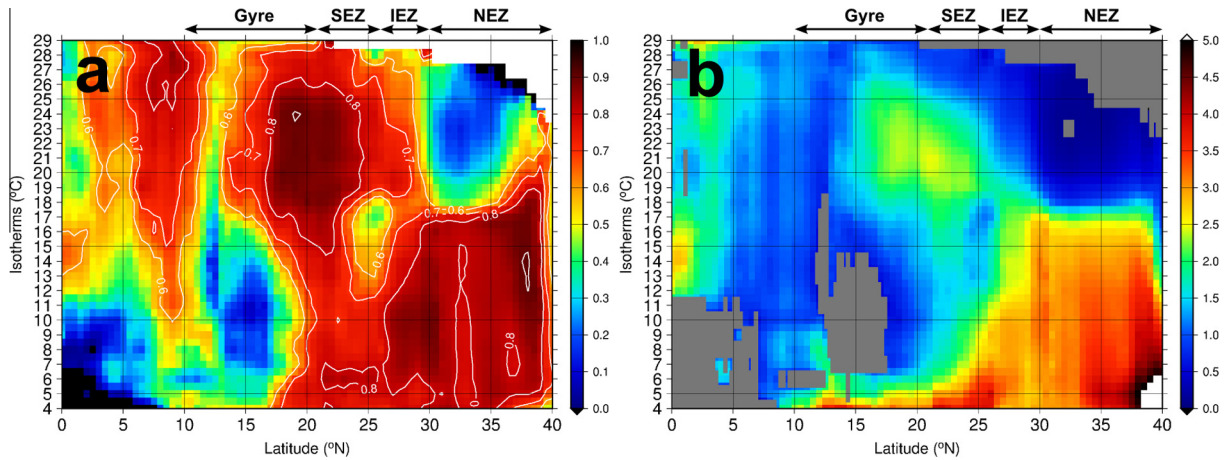


Fig. 5. (a) The isotherm-SSHA correlation from the equator to 40°N along 145°E in September. (b) Same as in (a), but for the slope of the regression. The slope less than 99% significance is marked in grey. The latitudinal band for the Gyre, SEZ, IEZ and NEZ are indicated.

produce 2.5 m variation in D20. The offset (*b*) is generally negative (Fig. 4b). Fig. 4c shows the correlation in September. Basically, the correlation between SSHA and D20 is high (~0.7). However, low correlation can be found in local regions to the north.

Fig. 5a illustrates the isotherm-SSHA correlation from the equator to 40°N along 145°E in September, to demonstrate the relationship in the vertical direction. It can be found that the correlation pattern varies significantly with isotherm and latitude. Basically, the correlation pattern is roughly consistent with the four zones (Fig. 1), but small-scale spatial variability still exists. Fig. 5b shows the corresponding cross section for the slope of the regression. The steepest slope is found in the lower isotherms (i.e., D4–D17) in the IEZ and NEZ, in which the slope is up to ~4–5 m cm⁻¹. It also corresponds to the high correlation area found in Fig. 5a. In the Gyre and SEZ, the larger slope of ~2.5 m cm⁻¹ is found in the upper isotherms (typically ~D25–D19). The grey regions in Fig. 5b are locations where slope does not meet the 99% statistical significance level and no retrieval on these regions is performed.

After obtaining the 26 isotherms, the OTS derivation is completed through inclusion of the satellite-observed SST (Section 2) and climatological monthly mixed layer depth (MLD) from the U.S. Naval Research Laboratory (NRL; Kara et al., 2002). Thus, the OTS from surface to the depth of ~1000 m (i.e., D4) can be obtained, and can be compared to the two isotherms based on the

existing method (Fig. 6). Hereafter, this regression method is referred to as the “REGWNP” (regression for the western North Pacific). It should be noted that the derived OTS is regular temperature, not potential temperature. Given the daily SSHA and SST maps, the corresponding daily OTS can be derived through the monthly regression, climatological isotherm depths and MLD within the same month. Fig. 7 displays exemplary profile comparison in September 2010 from the REGWNP (green curves), Argo (black curves) and TLM (red curves) in the four zones. It can be seen that the REGWNP profiles are generally much closer to the *in situ* Argo profiles, as compared to those from the TLM. Detailed validation results are presented in Section 5.

5. Validation and comparison with the TLM

An independent set of 7036 Argo profiles from the 2009 and 2010 typhoon seasons were used to validate the regression-derived OTS. The locations of these profiles are shown in Fig. 1a as blue dots. Series of validation for the REGWNP were conducted, and comparison with the existing TLM was made. Root-mean-square differences (RMSDs), biases, and errors were calculated between the observed (i.e., Argo profiles) and the REGWNP-derived isotherms to quantify the performance of the REGWNP. Here, error is defined as the percentage of RMSD in the observed mean:

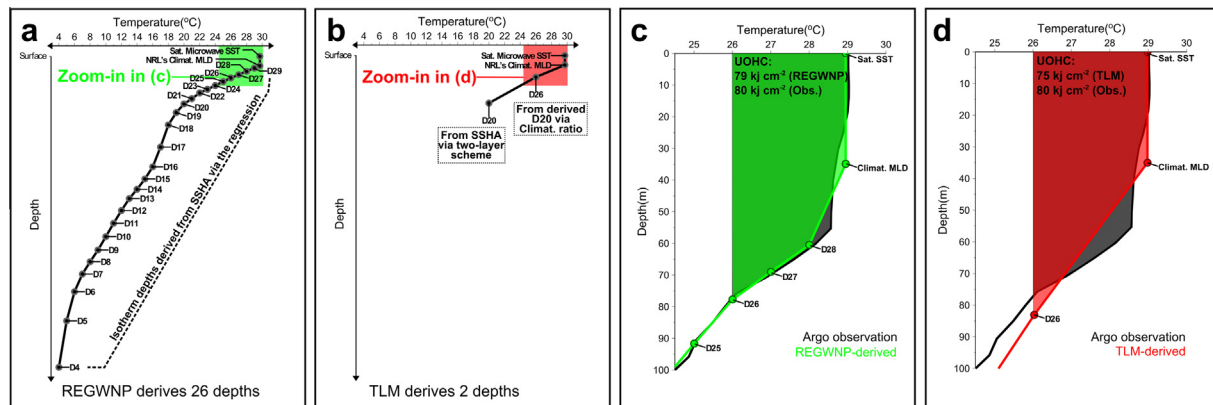


Fig. 6. Schematic of (a) REGWNP-derived profile and (b) TLM-derived profile. (c) Zoom-in area of (a) compares the profiles from the REGWNP (green) and Argo (black). (d) Zoom-in area of (b) compares the profiles from the TLM (red) and Argo (black). Shaded areas in (c) and (d) indicate the UOHC, their values are also shown. (For interpretation of the references to color in this figure legend, the reader is referred to the web version of this article.)

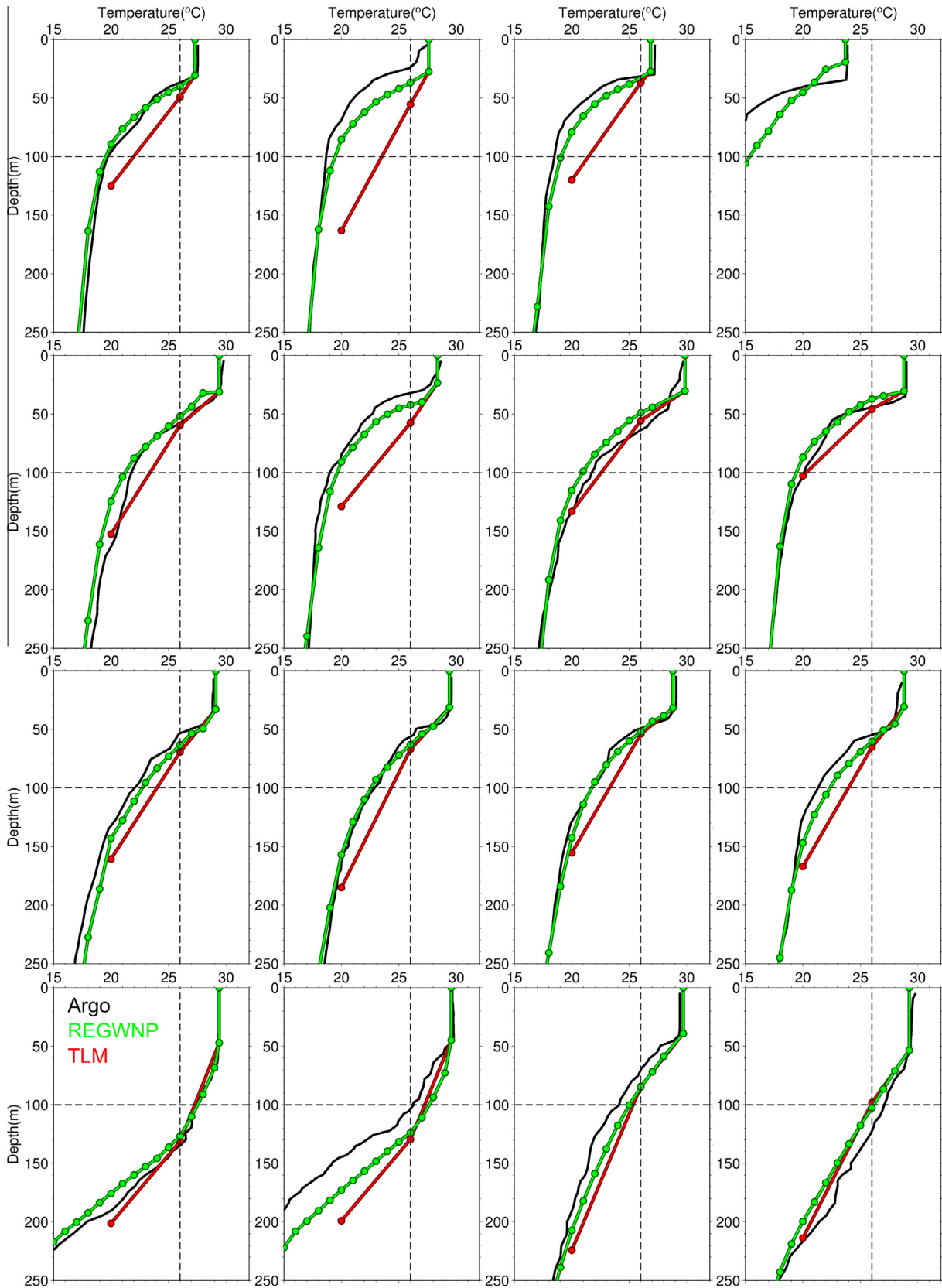


Fig. 7. Comparison between the profiles from the REGWNP (green), TLM (red) and Argo (black). From the upper to lower rows represent the profiles in the NEZ, IEZ, SEZ and Gyre. Each zone has four randomly-selected profiles in September of 2010. The TLM profile is not available in the upper right plot. The horizontal and vertical dashed lines depict 26 °C and the depth of 100 m, respectively. (For interpretation of the references to color in this figure legend, the reader is referred to the web version of this article.)

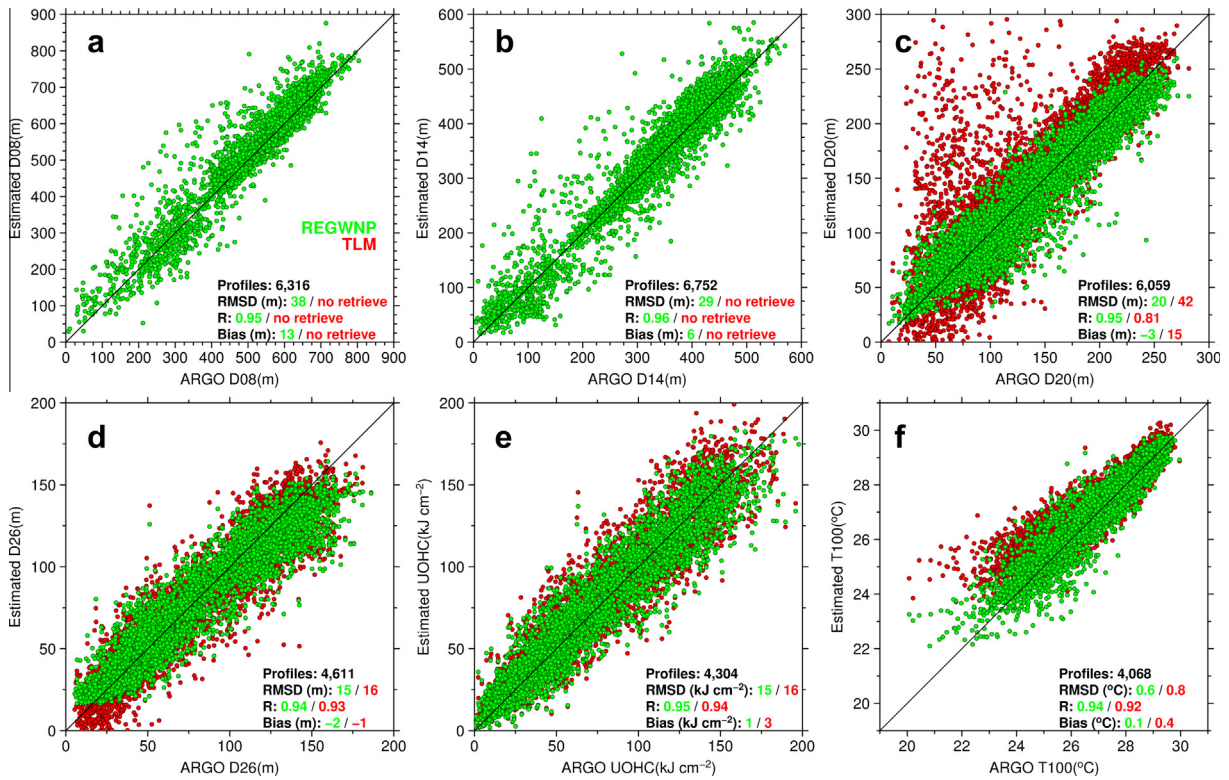


Fig. 8. Scatter plots of the REGWNP (green) and TLM (red) against Argo observations for (a) D8, (b) D14, (c) D20, (d) D26, (e) UOHC, and (f) T100 for all four zones (the Gyre, SEZ, IEZ and NEZ). The Argo profiles compared are from May–October of 2009–2010 (blue dots in Fig. 1a). Sample number, RMSD, correlation and bias with respect to Argo are shown. The TLM cannot derive D8 in (a) and D14 in (b). (For interpretation of the references to color in this figure legend, the reader is referred to the web version of this article.)

$$\text{Error} = \frac{\text{RMSD}}{\text{Mean}_{\text{obs}}} \times 100\%, \quad (3)$$

In addition to the derived isotherms, two other typhoon-intensification-related parameters calculated from the isotherms were also calculated and validated. These parameters are T100 (top 100-m averaged ocean temperature; Price, 2009) and tropical cyclone heat potential [TCHP; also called upper ocean heat content (UOHC)] (Leipper and Volgenau, 1972; Shay et al., 2000; Goni and Trinanes, 2003; Goni et al., 2009; Shay and Brewster, 2010). From Shay et al. (2000) and Goni and Trinanes (2003), TCHP (or UOHC) is the heat content exceeding 26 °C in the ocean. It can be calculated from the derived-OTS profile using:

$$\text{UOHC} = c_p \rho \int_0^{D26} \Delta T(z) dz, \quad (4)$$

where c_p is the heat capacity of the water at the constant pressure of 4178 J kg⁻¹ °C⁻¹, ρ is the average density of the upper ocean taken as 1026 kg m⁻³, and ΔT is the difference between $T(z)$ and 26 °C at the depth z .

For the comparison with the TLM, OTS is also calculated by the TLM. First, D20 is derived from SSHA through the two-layer reduced gravity scheme proposed by Goni et al. (1996) and Shay et al. (2000):

$$D20 = \overline{D20} + \frac{\rho_2}{\rho_2 - \rho_1} \eta, \quad (5)$$

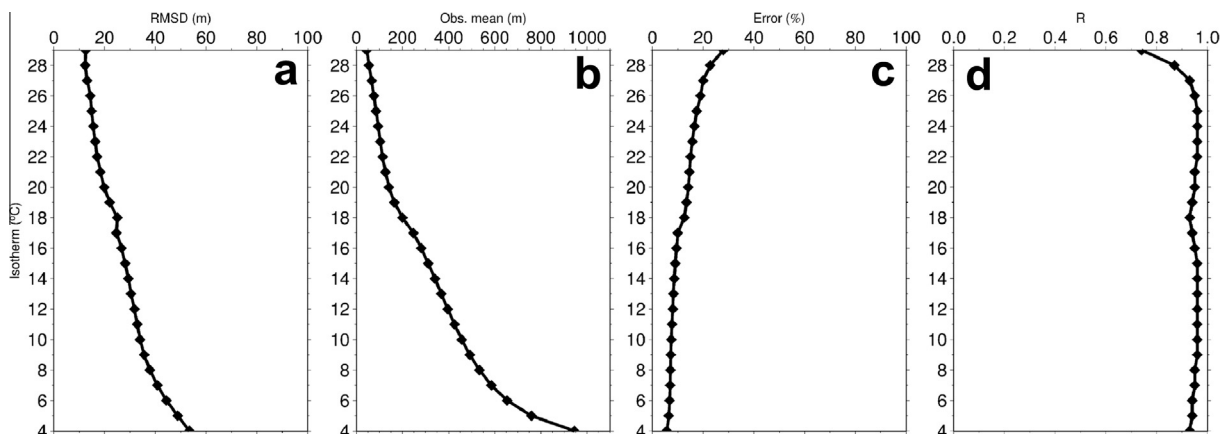


Fig. 9. (a) Overall RMSD of REGWNP-derived isotherms from D29–D4 over all four zones (the Gyre, SEZ, IEZ and NEZ) during May–October of 2009–2010. (b) Same as (a) but for observed mean depth of isotherms from Argo. (c) Same as (a), but for error of REGWNP-derived isotherms. (d) Same as (a), but for correlation between REGWNP-derived and Argo isotherms.

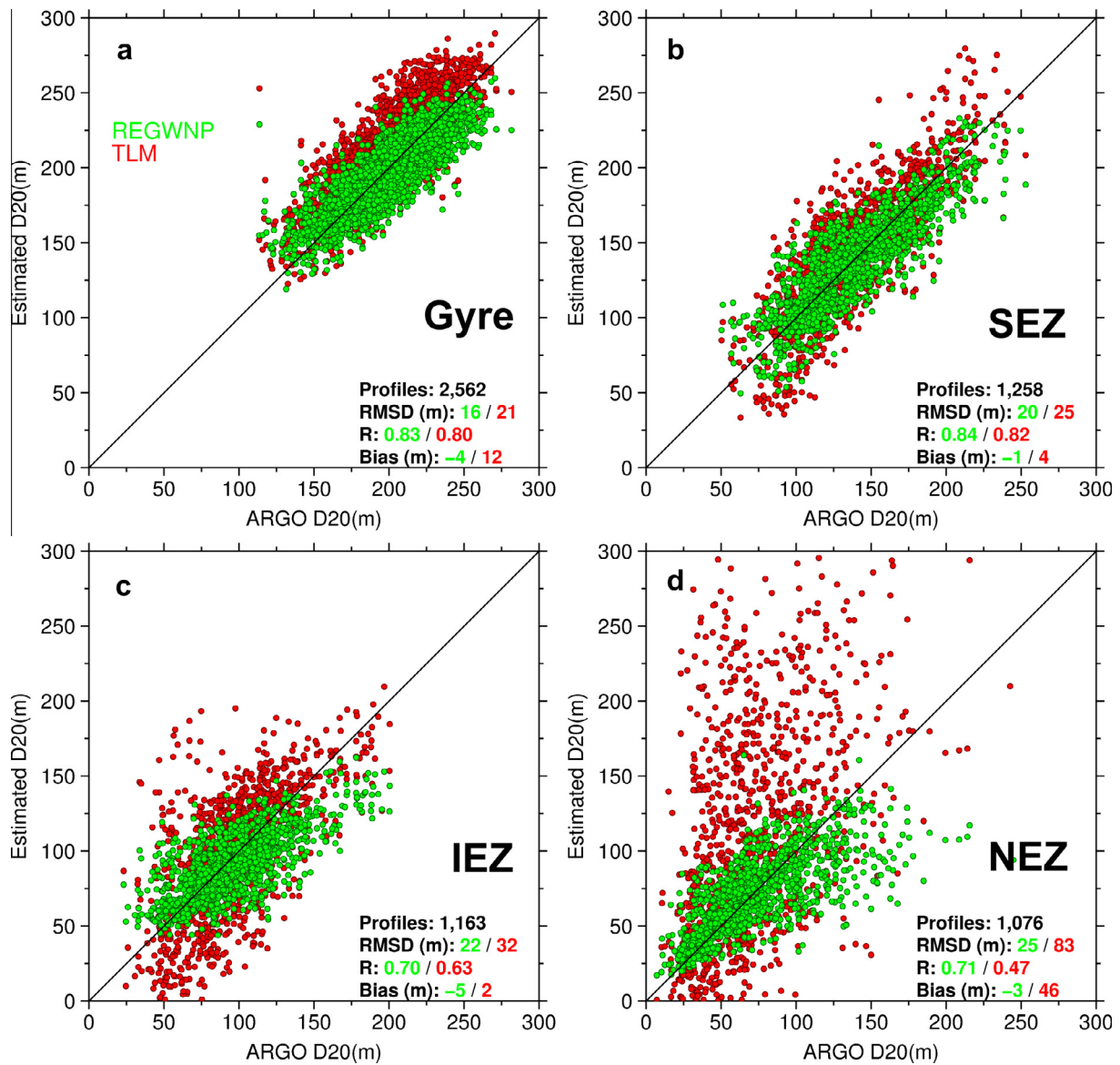


Fig. 10. Regional D20 scatter plots of the REGWNP (green) and TLM (red) against Argo observations for the (a) Gyre, (b) SEZ, (c) IEZ, and (d) NEZ. The Argo profiles compared are from May–October of 2009–2010 (blue dots in Fig. 1a). Sample number, RMSD, correlation and bias with respect to Argo are shown. (For interpretation of the references to color in this figure legend, the reader is referred to the web version of this article.)

where $\overline{D20}$, ρ_1 and ρ_2 are the climatological D20, upper layer and lower layer densities, respectively, which are obtained from the WOA01 monthly climatology fields. After obtaining D20, D26 is derived by multiplying a climatological ratio (D26/D20) from the WOA01. Finally, OTS is obtained with the satellite SST and NRL's monthly climatological MLD (Fig. 6b). More detailed information about TLM derivation in the WNPO can be found in Pun et al. (2007).

5.1. General validation

Fig. 8 shows that the REGWNP-derived isotherms (green dots) are reasonably constrained in RMSD with no evident biases. For the two well-known typhoon-related isotherms used in the TLM (Leipper and Volgenau, 1972; Shay et al., 2000; Goni and Trinanes, 2003; Lin et al., 2008), i.e., D26 and D20, the RMSDs (their biases) are 15 m (–2 m) and 20 m (–3 m), respectively, as shown in Fig. 8c and d. In comparison, there are significantly larger

biases (i.e., over-estimation) derived from the existing TLM for D20 (red dots in Fig. 8c), which was also pointed out by Pun et al. (2007). For the D20 from the TLM, the RMSD is as large as 42 m (i.e., twice the RMSD of the REGWNP). The performance of D26 from the TLM is better than that of D20, though its RMSD is still larger than those from the REGWNP (Fig. 8d). In terms of TCHP (or UOHC) and T100, it can be seen that though the REGWNP performs better than the TLM, both can obtain reasonable derivation, with RMSD being ~ 15 – 16 kJ cm^{-2} for UOHC and ~ 0.6 – 0.8 $^{\circ}\text{C}$ for T100 (Fig. 8e and f).

Because the REGWNP can derive 26 isotherms, we validate the rest of the isotherms as well. Fig. 8a and b depict the scatter plots for the two deeper isotherms, i.e., D8 and D14, while the complete validation for all 26 isotherms are summarized in Fig. 9. As in Fig. 8a and b, the RMSD for the lower isotherms are also reasonably constrained with most dots fall near the 1:1 diagonal line between the observed and the derived values. For D14 (D8), the RMSD is 29 m (38 m). Because these are deeper isotherms, located at

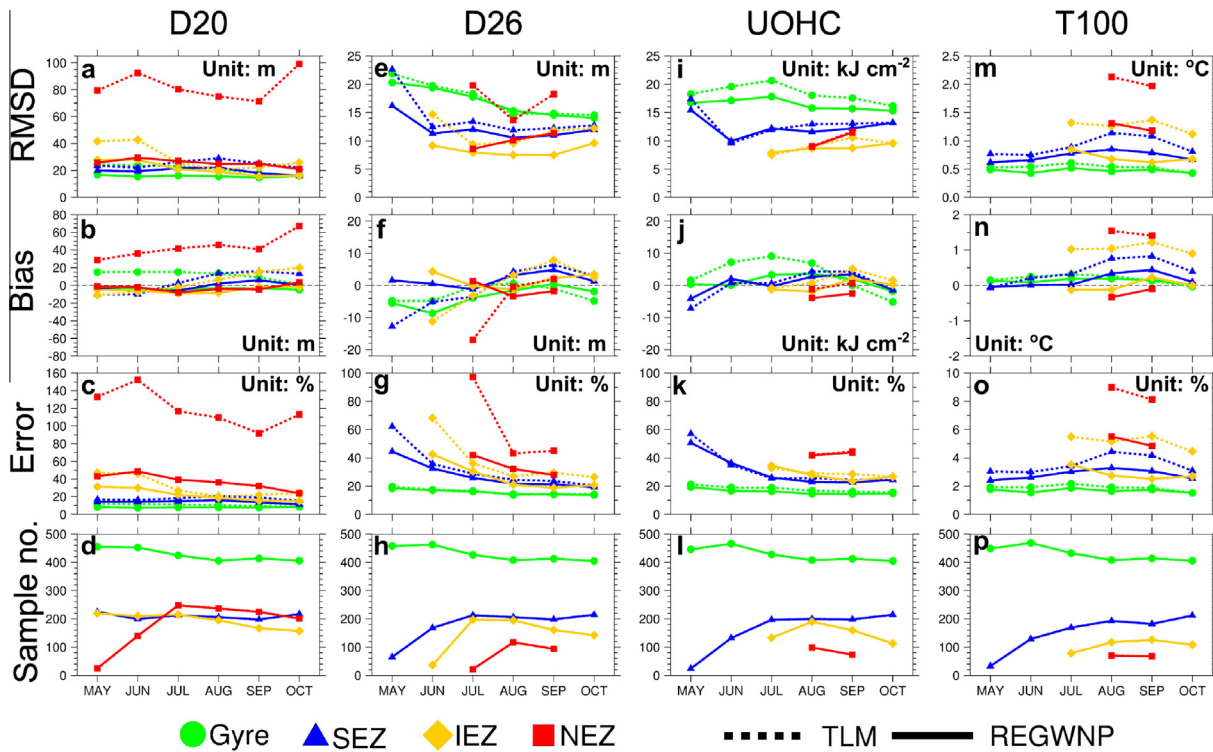


Fig. 11. Monthly RMSD (1st row), bias (2nd row), error percentage (3rd row), and sample number (4th row) for the REGWNP-derived D20 (1st column from the left), D26 (2nd column), UOHC (3rd column), and T100 (4th column). Green, blue, orange and red curves represent the Gyre, SEZ, IEZ and NEZ, respectively. Dashed and solid curves represent the TLM and REGWNP, respectively. The units for RMSD, bias, and error are shown. (For interpretation of the references to color in this figure legend, the reader is referred to the web version of this article.)

~400 m and 900 m (Fig. 9b), the errors (in terms of RMSD/observed mean) are actually smaller (Fig. 9c). It can be seen that for the deeper isotherms of D18 and below, the errors can be constrained to within 5–10%. For the upper ocean, the errors are larger, though they are still within 20% (Fig. 9c).

The quality of the REGWNP-derived isotherms can also be seen from Fig. 9d, which depicts the correlation between the derived and the observed isotherms. High correlation of ~0.9 exists for all isotherms but the very top isotherms of D28 and D29 near the mixed layer. Fig. 9d also illustrates one important point, that is, though traditionally only D20 and D26 are derived using satellite altimetry (Shay et al., 2000; Goni and Trinanes, 2003), many other isotherms can also be derived with as good, or even better, accuracy. This is encouraging because high-resolution and much more complete subsurface information can be derived from the REGWNP. As will be shown in Section 6, this improvement can lead to more accurate estimation of air–sea enthalpy (latent heat + sensible heat) flux and typhoon-induced ocean cooling, both are critical quantities for research that concerns typhoon intensification and typhoon–ocean interaction (Price, 1981, 2009; Emanuel, 1999; Bender and Ginis, 2000; Cione and Uhlhorn, 2003; Emanuel et al., 2004; Lin et al., 2005, 2009a, 2013; Cione et al., 2013).

Further, it can be seen that the isotherm derivation is not restricted to the upper ocean, but can be extended to deeper ocean (i.e., D4, typically ~1000 m; see Figs. 1b–1e and 9b). This suggests that the ocean thermal profiles derived from the REGWNP can also be applied to other scientific issues in oceanography over the WNPO, not just in the field of typhoon–ocean interaction that typically takes place in the top 300 m (Price, 1981, 2009; Lin et al., 2005; D’Asaro et al., 2011; Lin, 2012; Mrvaljevic et al., 2013).

5.2. Regional and monthly validations

In addition to general validation, regional validation is performed to assess the accuracy in different parts of the WNPO (Fig. 1a). This provides additional information on the regional dependence of the performance; especially, it was noted by Pun et al. (2007) that the D20 from the TLM suffers large over-estimation over the NEZ region. Fig. 10 depicts the results of D20 derivation. It can be seen that for the two zones at the southern part of the WNPO, i.e., Gyre and SEZ, the REGWNP is well constrained with RMSD of 16 m and 20 m, respectively (green dots in Fig. 10a and b). Towards the northern part of the WNPO, i.e., the IEZ and the NEZ regions, the RMSD increases to 22 m and 25 m and the correlation of ~0.7 is also lower than that in the Gyre and the SEZ regions (with correlation ~0.83–0.84). This shows that the performance of the REGWNP is better over the southern WNPO (south of 26°N) than over the northern part (Fig. 1a). As reported by Pun et al. (2007) and in the SOM, the northern regions are more complex oceanographically, including regions where the Oyashio and the Kuroshio meet and the Kuroshio meanders (Yasuda et al., 1992; Qiu, 1999). It is therefore understandable that satellite SSHA derivation does not perform as well as it does in the southern regions.

The same situation is found in the TLM, but the northern degradation in performance is much more severe (red dots in Fig. 10c and d). It can be seen that the RMSD of 83 m over the NEZ is more than 300% as compared to the REGWNP method (RMSD 25 m) (Fig. 10d). Also, very large biases (over-estimation) of 46 m are found in the TLM, as compare to the small bias of -3 m in the REGWNP. Using the TLM, the correlation between the observed and the derived D20 drops to 0.47, as compared to the higher correlation of 0.71 found using the REGWNP (Fig. 10d). As quantified in Fig. 11c,

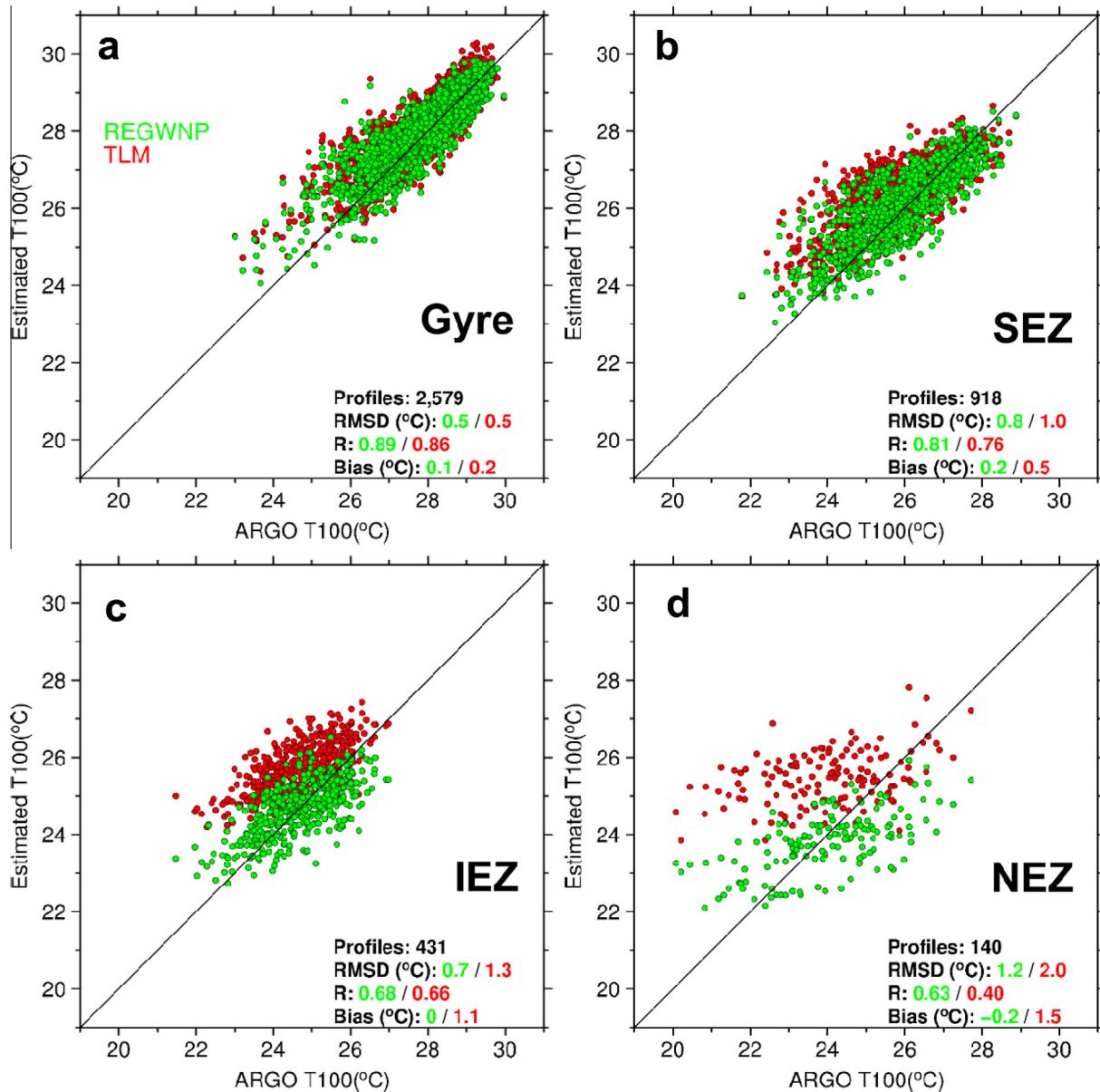


Fig. 12. Same as in Fig. 10, but for T100.

this is equivalent to more than 100% error (red dashed curve), as compared to the ~30% error (red solid curve) for the REGWNP method. Over the two southern regions, the performance of the TLM is much better, though it is still not as good as that of the REGWNP (Fig. 10a and b).

The above comparison shows the regional dependence of the performance in D20 derivation. Over the southern regions, both the REGWNP and the TLM are usable, though the REGWNP has higher accuracy. Over the northern region, the REGWNP has less accuracy and should be used with caution (Figs. 10 and 11). It is not advisable to use the TLM over the two northern regions, given the low performance. Similar situation is also found in T100 estimation (Fig. 12).

Quantification of the regional performance for D20, D26, UOHC, and T100 using both methods is given in Fig. 11. Also, temporal performance is assessed. In general, there is less accuracy in the earlier typhoon season (i.e., May and June) for both methods.

And the best performance for both methods is found in July–September (3rd row in Fig. 11).

6. Discussion

6.1. Applicability of REGWNP-derived typhoon-related parameters

According to the validation (Section 5), it is evident that the REGWNP can reasonably estimate the typhoon-related parameters: D20, D26, UOHC and T100 in the WNPO. As a convenient guide, we experimentally took 35% of error as a threshold to determine whether the parameters derived by the REGWNP are of acceptable accuracy. Fig. 13 shows the applicable zones and months of the REGWNP for each typhoon-related parameter. It can be seen that REGWNP is well applicable in the Gyre throughout the May–October typhoon season. Similar applicability is also

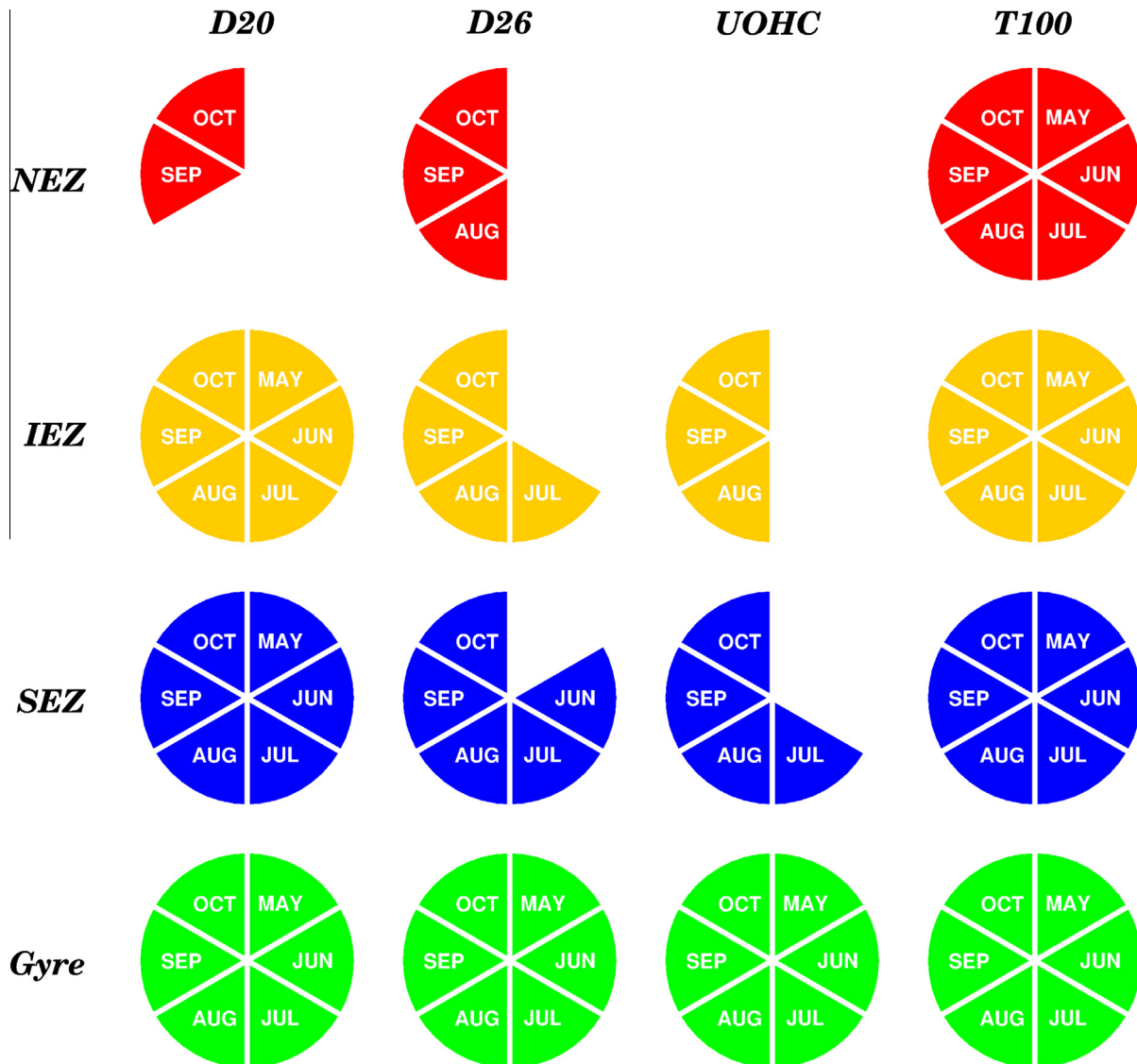


Fig. 13. Applicability chart for REGWNP-derived D20, D26, UOHC and T100 for typhoon applications. From upper to lower rows are for the NEZ, IEZ, SEZ and Gyre, respectively. The months, May–October, are indicated in each pie chart. The applicability threshold is defined as an error of 35%.

found in the SEZ, except some part of the early season (i.e., May and June). Due to colder OTS in the earlier typhoon season (May and June) in the two northern zones (i.e., NEZ and IEZ), the error is larger because the mean values are usually small (see Eq. (3)). Therefore, for these northern zones, it is more difficult to achieve <35% error.

6.2. Improvement on SST cooling and enthalpy flux estimations

When considering ocean's control over typhoon intensity change, the most important quantities to be obtained are the during-typhoon SST cooling and air–sea enthalpy (latent heat + sensible heat) fluxes (Emanuel, 1999; Bender and Ginis, 2000; Cione and Uhlhorn, 2003; Emanuel et al., 2004; Lin et al., 2005, 2009a, 2013; Cione et al., 2013). Though *in situ* sampling has been much improved through the Argo float deployments (Gould et al., 2004), *in situ* ocean observation is still very sparse over the vast ocean. Especially, when operational modeling and forecasting are concerned, it is often difficult to find *in situ* observations near the typhoon track (Lin et al., 2005, 2008, 2009b; D'Asaro et al., 2011; Pun et al., 2011). Satellite-derived OTS thus provides critical com-

plementary information because it can provide synoptic OTS maps, instead of point-wise *in situ* observations.

To obtain accurate forecast of typhoon intensity change, as accurate as possible during-typhoon SST cooling and enthalpy fluxes are needed, because ocean is the energy source for typhoon's intensification (Emanuel, 1999; Bender and Ginis, 2000; Emanuel et al., 2004). Pre-typhoon OTS profiles along the typhoon track are thus needed as input to predict the during-typhoon SST cooling and enthalpy fluxes. In the often absence of *in situ* profiles, satellite-derived profiles can be used. Fig. 14 compares the performance of the two satellite-derived methods, using the co-incident and co-located Argo profiles depicted in Fig. 7 as the truth. Using these profiles as input to an ocean mixed layer model (Mellor and Yamada, 1982), the performance is assessed. Here, the drag coefficient (C_d) used in the SST-cooling prediction is the high wind coefficient (suitable under typhoon condition) from Powell et al. (2003). All simulations are performed under typhoon translation speed (i.e., U_h) of 5 m s^{-1} because it is the averaged U_h observed in the WNPO during typhoon intensification (Lin et al., 2008, 2009b). Typhoon wind forcing from $35\text{--}65 \text{ m s}^{-1}$ with an interval of 5 m s^{-1} is used, so that all possible wind speeds from Categories 1 to 5 conditions

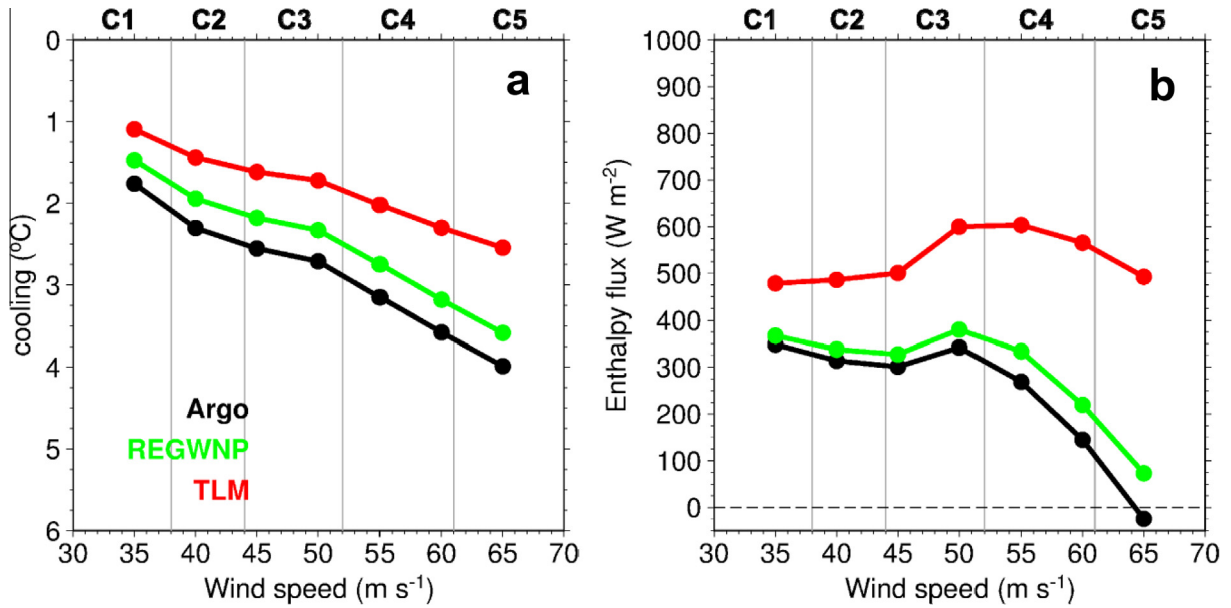


Fig. 14. (a) SST cooling and (b) enthalpy flux comparisons between using the TLM (red curves), REGWNP (green curves), and Argo (black curves) profiles as input to the mixed-layer model. The results shown in (a) and (b) are the average of 16 profiles (Fig. 7) runs. The Saffir–Simpson typhoon scale from Categories 1–5 based on the 10-min maximum sustained winds is depicted. (For interpretation of the references to color in this figure legend, the reader is referred to the web version of this article.)

Table 2
SST cooling assessment from 16 profiles (Fig. 7) as input to the ocean mixed layer model. Unit is in °C.

Wind speed (m s ⁻¹)	35	40	45	50	55	60	65	Average
TLM	1.09	1.44	1.62	1.72	2.02	2.30	2.54	1.82
REGWNP	1.47	1.94	2.18	2.33	2.75	3.18	3.58	2.49
Argo	1.76	2.30	2.56	2.71	3.15	3.58	3.99	2.86

can be simulated. Further detail in the methodology can be found in Lin (2012).

After obtaining the SST cooling, the enthalpy flux, i.e., the sensible (Q_s) plus latent (Q_l) heat fluxes, under typhoon condition can be estimated using the bulk aerodynamic formulas (Cione and Uhlhorn, 2003; Jacob and Shay, 2003; Powell et al., 2003; Black et al., 2007; Lin et al., 2009b, 2013) as follows.

$$Q_s = C_H W (T_s - T_a) \rho_a C_{pa}, \tag{6}$$

$$Q_l = C_E W (q_s - q_a) \rho_a L_{va}, \tag{7}$$

where C_H and C_E are the exchange coefficients of sensible and latent heat, respectively; W is the wind speed; T_s and T_a are SST and near-surface air temperature, respectively. T_s is the during-typhoon SST, calculated as initial SST minus SST cooling; T_a is taken as a constant of 27 °C; q_s and q_a are surface and air specific humidity, respectively; and ρ_a , C_{pa} , and L_{va} are air density, heat capacity of the air, and latent heat of vaporization, respectively.

Fig. 14 shows that for all wind speeds, the REGWNP (green curves) predicts more accurate during-typhoon SST cooling and enthalpy fluxes than the TLM (red curves). It also shows that the TLM underestimates the during-typhoon SST cooling (Fig. 14a) and results in significant over-estimation in the enthalpy fluxes (Fig. 14b). Table 2 quantifies the performance. It can be observed that on average the during-typhoon SST difference between the REGWNP and Argo is limited to 0.37 °C, but the average difference between the TLM and Argo is 1.04 °C.

Table 3
Enthalpy flux assessment from the SST cooling of 16 profiles (Fig. 7). Unit is in W m⁻².

Wind speed (m s ⁻¹)	35	40	45	50	55	60	65	Average
TLM	479	486	501	600	604	565	492	532
REGWNP	367	338	327	380	334	220	73	291
Argo	348	314	301	342	269	145	-25	242

Since the average SST cooling using Argo floats is 2.86 °C, the corresponding error for the REGWNP would be 13% (0.37 °C/2.86 °C) and 36% for the TLM (1.04 °C/2.86 °C) (Table 2). As for the enthalpy fluxes, the average difference between REGWNP and Argo is 49 W m⁻², but the difference between the TLM and Argo increases to 290 W m⁻². Since the averaged enthalpy flux from the Argo is 242 W m⁻², the equivalent error between REGWNP and Argo would be 20% (49 W m⁻²/242 W m⁻²), while the error between the TLM and Argo is 120% (290 W m⁻²/242 W m⁻²) (Table 3).

Exploring the possible reason for the poor performance of the TLM derived profile, one possibility is the coarse vertical resolution (Fig. 6). Since only two isotherms are used to characterize OTS; but for SST cooling estimation, a more complete vertical ocean thermal structure is required. Therefore, interpolation and extrapolation are involved. In other words, since the TLM only provides D20 and D26, the rest of the thermal structure is obtained through interpolation and extrapolation of D20 and D26. As shown by Fig. 15, this can lead to significant deviation

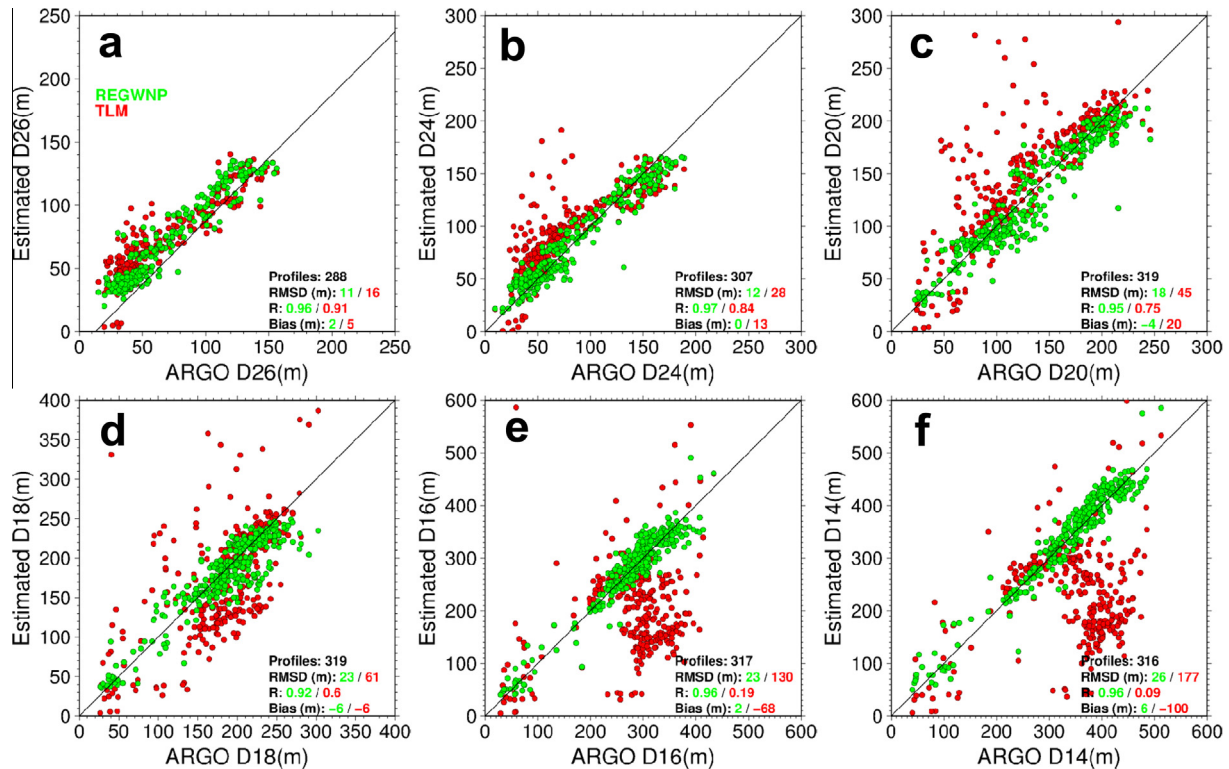


Fig. 15. Comparisons of (a) D26, (b) D24, (c) D20, (d) D18, (e) D16 and (f) D14 between the REGWNP (green dots) and TLM (red dots) and Argo observations in September of 2010. D24, D18, D16 and D14 are obtained by interpolation or extrapolation for the TLM. Sample number, RMSD, correlation and bias with respect to Argo are shown. (For interpretation of the references to color in this figure legend, the reader is referred to the web version of this article.)

from reality (see the red dots). As for the REGWNP method, since each isotherm is derived individually, the accuracy is much higher and closer to the Argo observations (see the green dots in Fig. 15).

7. Conclusion

Though the importance of ocean's subsurface thermal structure in tropical cyclone's intensity change has been known since 1970s, it was difficult to obtain subsurface information over the vast oceans with limited *in situ* point-wise observations. Only since the launch of satellite altimetry in 1993 and the pioneering work (i.e., the TLM) of Goni et al. (1996) and Shay et al. (2000), it was possible to operationally derive synoptic ocean subsurface thermal structure using altimetry for typhoons intensity forecasting and research.

However, as sciences progress it is desirable to improve vertical characterization of OTS, after all the use of only two isotherms in the TLM is indeed too coarse. With the deployment of Argo floats in 2000, there has been a quantum jump in ocean subsurface sampling. Therefore it has become possible now to combine this large amount of *in situ* profiles with satellite altimetry to regression and develop new generation of derivation. Based on this method, we derive a maximum of 26 isotherms (from D4 to D29) to improve the vertical characterization (Fig. 6). With these high resolution profiles, the shape of ocean subsurface thermal structure can be well-characterized. Using an independent set of more than 7000 Argo profiles for validation, it is found that this new generation of derivation is of good accuracy for all isotherms with error mostly below 15% (Fig. 9c). Because many more isotherms can be used, evident improvement in subsequent parameters derived or estimated using these satellite-derived profiles is achieved. Improvement is found in all related parameters, including T100, UOHC,

during-typhoon SST cooling, and air–sea enthalpy flux estimation (Figs. 7–15).

Further validation on the regional dependence found that the performance is better over the southern part of the WNPO (i.e., at the south of 26°N), co-located with the main development region of typhoons in the WNPO. Over the northern region, the performance degrades by about 20% in error (i.e., 30–40%). Similar northern degradation in performance is also found in the traditional TLM but is much more severe. As in Fig. 11, the error found in the TLM for D20 can be more than 100%. Therefore, over the northern WNPO (i.e., at the north of 26°N, especially over the NEZ), it should be cautious in using the satellite-derived OTS information.

Finally, as this new generation of derivation can be extended to D4, i.e., ~1000 m, the application of satellite-derived OTS is not limited to typhoon–ocean interaction application, but can be extended to new oceanographic issues because information from deeper ocean can be obtained.

Acknowledgements

The authors appreciate the Argo team for the *in situ* temperature profiles, the AVISO team for the SSHA data, the RSS team for the SST data, and the NOAA/NODC for the climatological ocean temperature data. The authors sincerely thank Dr. Jim Price of Woods Hole Oceanographic Institution (WHOI) and three anonymous reviewers for their valuable comments and suggestions. With their helps, this work is able to be accomplished. Thanks also to US Office of Naval Research (ONR) and WHOI, part of this work was done when Iam-Fei Pun was working at WHOI, supported by ONR. Iam-Fei Pun is supported by Grants NSC 102-2811-M-002-095 and ONR N00014-11-1-0394. I.-I. Lin is supported by Grants NSC 101-2111-M-002-002-MY2 and NSC 101-2628-M-002-001-

MY4. Dong S. Ko is supported by ONR ITOP program under Contract N00014-08WX-2-1170.

Appendix A. Supplementary material

Supplementary data associated with this article can be found, in the online version, at <http://dx.doi.org/10.1016/j.pocan.2013.10.004>.

References

- Balaguru, K., Chang, P., Saravanan, R., Leung, L.R., Xu, Z., Li, M., Hsieh, J.S., 2012. Ocean barrier layers' effect on tropical cyclone intensification. *Proceedings of the National Academy of Sciences of the United States of America* 109 (36), 14343–14347.
- Bender, M.A., Ginis, I., 2000. Real-case simulations of hurricane–ocean interaction using a high-resolution coupled model: effects on hurricane intensity. *Monthly Weather Review* 128, 917–946.
- Bender, M.A., Ginis, I., Kurihara, Y., 1993. Numerical simulations of tropical cyclone–ocean interaction with a high-resolution coupled model. *Journal of Geophysical Research – Atmospheres* 98, 23245–23263.
- Black, P.G., D'Asaro, E.A., Drennan, W.M., French, J.R., Niiler, P.P., Sanford, T.B., Terrill, E.J., Walsh, E.J., Zhang, J.A., 2007. Air–sea exchange in hurricanes: synthesis of observations from the coupled boundary layer air–sea transfer experiment. *Bulletin of the American Meteorological Society* 88, 357–374.
- Carnes, M.R., Mitchell, J.L., Dewitt, P.W., 1990. Synthetic temperature profiles derived from Geosat altimetry – comparison with air-dropped expendable bathythermograph profiles. *Journal of Geophysical Research – Oceans* 95, 17979–17992.
- Cazenave, A., Remy, F., 2011. Sea level and climate: measurements and causes of changes. *WIREs Climate Change* 2, 647–662.
- Chang, S.W., Anthes, R.A., 1978. Numerical simulations of oceans non-linear, baroclinic response to translating hurricanes. *Journal of Physical Oceanography* 8, 468–480.
- Chelton, D.B., Schlax, M.G., Samelson, R.M., 2011. Global observations of nonlinear mesoscale eddies. *Progress in Oceanography* 91, 167–216.
- Cheney, R.E., 1982. Comparison data for Seasat altimetry in the western North-Atlantic. *Journal of Geophysical Research – Oceans and Atmospheres* 87, 3247–3253.
- Cione, J., Uhlhorn, E., 2003. Sea surface temperature variability in hurricanes: implications with respect to intensity change. *Monthly Weather Review* 131, 1783–1796.
- Cione, J., Kalina, E., Zhang, J., Uhlhorn, E., 2013. Observations of air–sea interaction and intensity change in hurricanes. *Monthly Weather Review* 141, 2368–2382.
- D'Asaro, E., Black, P., Centurioni, L., Harr, P., Jayne, S., Lin, I.I., Lee, C., Morzel, J., Mrvaljevic, R., Niiler, P., Rainville, L., Sanford, T., Tang, T.Y., 2011. Typhoon–ocean interaction in the western North Pacific, Part 1. *Oceanography* 24, 24–31.
- Ducet, N., Le Traon, P.Y., Reverdin, G., 2000. Global high-resolution mapping of ocean circulation from TOPEX/Poseidon and ERS-1 and-2. *Journal of Geophysical Research – Oceans* 105, 19477–19498.
- Emanuel, K.A., 1999. Thermodynamic control of hurricane intensity. *Nature* 401, 665–669.
- Emanuel, K., DesAutels, C., Holloway, C., Korty, R., 2004. Environmental control of tropical cyclone intensity. *Journal of the Atmospheric Sciences* 61, 843–858.
- Fu, L.L., Stammer, D., Leben, B.B., Chelton, D.B., 2003. Improved spatial resolution of ocean surface topography from the TOPEX/Poseidon – Jason-1 tandem altimeter mission. *EOS, Transaction, American Geophysical Union* 84, 247–248.
- Gallacher, P.C., Rotunno, R., Emanuel, K.A., 1989. Tropical cyclogenesis in a coupled ocean–atmosphere model. In: 18th Conference on Hurricanes and Tropical Meteorology. American Meteorological Society, Boston.
- Gill, A.E., Niiler, P.P., 1973. The theory of the seasonal variability in the oceans. *Deep-Sea Research* 20, 141–177.
- Gilson, J., Roemmich, D., Cornuelle, B., Fu, L.L., 1998. Relationship of TOPEX/Poseidon altimetric height to steric height and circulation in the North Pacific. *Journal of Geophysical Research – Oceans* 103, 27947–27965.
- Goni, G.J., Trinanes, J.A., 2003. Ocean thermal structure monitoring could aid in the intensity forecast of tropical cyclones. *EOS, Transaction, American Geophysical Union* 84, 573–580.
- Goni, G., Kamholz, S., Garzoli, S., Olson, D., 1996. Dynamics of the Brazil–Malvinas Confluence based on inverted echo sounders and altimetry. *Journal of Geophysical Research – Oceans* 101, 16273–16289.
- Goni, G., Demaria, M., Knaff, J., Sampson, C., Ginis, I., Bringas, F., Mavume, A., Lauer, C., Lin, I.I., Ali, M.M., Sandery, P., Ramos-Buarque, S., Kang, K., Mehra, A., Chassignet, E., Halliwell, G., 2009. Applications of satellite-derived ocean measurements to tropical cyclone intensity forecasting. *Oceanography* 22, 190–197.
- Gould, J., Roemmich, D., Wijffels, S., Freeland, H., Ignaszewesky, M., Jianping, X., Pouliquen, S., Desaubies, Y., Send, U., Radhakrishnan, K., Takeuchi, K., Kim, K., Danchenkov, M., Sutton, P., King, B., Owens, B., Riser, S., 2004. Argo profiling floats bring new era of in situ ocean observations. *EOS, Transaction, American Geophysical Union* 85 (19), 185–191.
- Gray, W.M., 1979. Hurricanes: their formation, structure and likely role in the tropical circulation. In: Shaw, D.B. (Ed.), *Meteorology Over the Tropical Oceans*. Royal Meteorological Society, pp. 155–218.
- Guinehut, S., Dhomp, A.L., Larnicol, G., Le Traon, P.Y., 2012. High resolution 3-D temperature and salinity fields derived from in situ and satellite observations. *Ocean Science* 9, 1313–1347.
- Holliday, C.R., Thompson, A.H., 1979. Climatological characteristics of rapidly intensifying typhoons. *Monthly Weather Review* 107, 1022–1034.
- Hong, X.D., Chang, S.W., Raman, S., Shay, L.K., Hodur, R., 2000. The interaction between Hurricane Opal (1995) and a warm core ring in the Gulf of Mexico. *Monthly Weather Review* 128, 1347–1365.
- Jacob, S.D., Shay, L.K., 2003. The role of oceanic mesoscale features on the tropical-cyclone induced mixed layer response. *Journal of Physical Oceanography* 33, 649–676.
- Kara, A.B., Rochford, P.A., Hurlburt, H.E., 2002. *Naval Research Laboratory Mixed Layer Depth (NMLD) Climatologies*. NRL Report No. NRL/FR/7330-02-9995, 26.
- Le Traon, P.Y., Dibarboure, G., 2004. Illustration of the contribution of the tandem mission to mesoscale studies. *Marine Geodesy* 27, 3–13.
- Leipper, D.F., Volgenau, D., 1972. Hurricane heat potential of the Gulf of Mexico. *Journal of Physical Oceanography* 2, 218–224.
- Lin, I.I., 2012. Typhoon-induced phytoplankton blooms and primary productivity increase in the western North Pacific subtropical ocean. *Journal of Geophysical Research – Oceans* 117, C03039.
- Lin, I.I., Liu, W.T., Wu, C.C., Chiang, J.C.H., Sui, C.H., 2003a. Satellite observations of modulation of surface winds by typhoon-induced upper ocean cooling. *Geophysical Research Letters* 30, 1131.
- Lin, I.I., Liu, W.T., Wu, C.C., Wong, G.T.F., Hu, C., Chen, Z., Liang, W.D., Yang, Y., Liu, K.K., 2003b. New evidence for enhanced ocean primary production triggered by tropical cyclone. *Geophysical Research Letters* 30, 1718.
- Lin, I.I., Wu, C.C., Emanuel, K.A., Lee, I.H., Wu, C.R., Pun, I.F., 2005. The interaction of Supertyphoon Maemi (2003) with a warm ocean eddy. *Monthly Weather Review* 133, 2635–2649.
- Lin, I.I., Wu, C.C., Pun, I.F., Ko, D.S., 2008. Upper-ocean thermal structure and the western North Pacific category 5 typhoons. Part I: ocean features and the category 5 typhoons' intensification. *Monthly Weather Review* 136, 3288–3306.
- Lin, I.I., Chen, C.H., Pun, I.F., Liu, W.T., Wu, C.C., 2009a. Warm ocean anomaly, air sea fluxes, and the rapid intensification of tropical cyclone Nargis (2008). *Geophysical Research Letters* 36, L03817.
- Lin, I.I., Pun, I.F., Wu, C.C., 2009b. Upper-ocean thermal structure and the western North Pacific category 5 typhoons. Part II: dependence on translation speed. *Monthly Weather Review* 137, 3744–3757.
- Lin, I.I., Black, P., Price, J.F., Yang, C.Y., Chen, S.S., Lien, C.C., Harr, P.A., Chi, N.H., Wu, C.C., D'Asaro, E.A., 2013. An ocean cooling potential intensity index for tropical cyclones. *Geophysical Research Letters* 40, 1878–1882.
- Mainelli, M., DeMaria, M., Shay, L.K., Goni, G., 2008. Application of oceanic heat content estimation to operational forecasting of recent Atlantic category 5 hurricanes. *Weather and Forecasting* 23, 3–16.
- Mellor, G.L., Yamada, T., 1982. Development of a turbulence closure-model for geophysical fluid problems. *Reviews of Geophysics* 20, 851–875.
- Moon, I.J., Kwon, S.J., 2012. Impact of upper-ocean thermal structure on the intensity of Korean peninsular landfall typhoons. *Progress in Oceanography* 105, 61–66.
- Mrvaljevic, R.K., Black, P.G., Centurioni, L.R., Chang, Y.T., D'Asaro, E.A., Jayne, S.R., Lee, C.M., Lien, R.C., Lin, I.I., Morzel, J., Niiler, P.P., Rainville, L., Sanford, T.B., 2013. Observations of the cold wake of Typhoon Fanapi (2010). *Geophysical Research Letters* 40, 316–321.
- Niiler, P.P., Maximenko, N.A., Panteleev, G.G., Yamagata, T., Olson, D.B., 2003. Near-surface dynamical structure of the Kuroshio extension. *Journal of Geophysical Research* 108, C6, 3193.
- Pascual, A., Faugere, Y., Larnicol, G., Le Traon, P.Y., 2006. Improved description of the ocean mesoscale variability by combining four satellite altimeters. *Geophysical Research Letters* 33, L02611.
- Pascual, A., Boone, C., Larnicol, G., Le Traon, P.Y., 2009. On the quality of real-time altimeter gridded fields: comparison with in situ data. *Journal of Atmospheric and Oceanic Technology* 26, 556–569.
- Powell, M.D., Vickery, P.J., Reinhold, T.A., 2003. Reduced drag coefficient for high wind speeds in tropical cyclones. *Nature* 422, 279–283.
- Price, J.F., 1981. Upper ocean response to a hurricane. *Journal of Physical Oceanography* 11, 153–175.
- Price, J.F., 2009. Metrics of hurricane–ocean interaction: vertically-integrated or vertically-averaged ocean temperature? *Ocean Science* 5, 351–368.
- Pun, I.F., Lin, I.I., Wu, C.R., Ko, D.H., Liu, W.T., 2007. Validation and application of altimetry-derived upper ocean thermal structure in the western North Pacific Ocean for typhoon-intensity forecast. *IEEE Transactions on Geoscience and Remote Sensing* 45, 1616–1630.
- Pun, I.F., Chang, Y.T., Lin, I.I., Tang, T.Y., Lien, R.C., 2011. Typhoon–ocean interaction in the western North Pacific: Part 2. *Oceanography* 24, 32–41.
- Pun, I.-F., Lin, I.-I., Lo, M.-H., 2013. Recent increase in high tropical cyclone heat potential area in the Western North Pacific Ocean. *Geophysical Research Letters* 40, 4680–4684.
- Qiu, B., 1999. Seasonal eddy field modulation of the North Pacific subtropical countercurrent: TOPEX/Poseidon observations and theory. *Journal of Physical Oceanography* 29, 2471–2486.
- Qiu, B., Chen, S.M., 2010. Interannual variability of the North Pacific Subtropical Countercurrent and its associated mesoscale eddy field. *Journal of Physical Oceanography* 40, 213–225.

- Roemmich, D., Riser, S., Davis, R., Desaubies, Y., 2004. Autonomous profiling floats: workhorse for broad-scale ocean observations. *Marine Technology Society Journal* 38, 21–29.
- Schade, L.R., Emanuel, K.A., 1999. The ocean's effect on the intensity of tropical cyclones: results from a simple coupled atmosphere–ocean model. *Journal of the Atmospheric Sciences* 56, 642–651.
- Shay, L.K., Brewster, J.K., 2010. Oceanic heat content variability in the eastern Pacific Ocean for hurricane intensity forecasting. *Monthly Weather Review* 138, 2110–2131.
- Shay, L.K., Goni, G.J., Black, P.G., 2000. Effects of a warm oceanic feature on Hurricane Opal. *Monthly Weather Review* 128, 1366–1383.
- Stephens, C., Antonov, J.I., Boyer, T.P., Conkright, M.E., Locarnini, R.A., O'Brien, T.D., Garcia, H.E., 2002. World Ocean Atlas 2001, vol. 1: temperature. In: Levitus, S. (Ed.), NOAA Atlas NESDIS 49. U.S. Government Printing Office, Washington, DC.
- Tseng, Y.-H., Jan, S., Dietrich, D.E., Lin, I.-I., Chang, Y.-T., Tang, T.Y., 2010. Modeled Oceanic Response and sea surface cooling to Typhoon Kai-Tak. *Terrestrial Atmospheric and Oceanic Sciences* 21, 85–98.
- Wentz, F.J., Gentemann, C., Smith, D., Chelton, D., 2000. Satellite measurements of sea surface temperature through clouds. *Science* 288, 847–850.
- White, W.B., Tai, C.K., 1995. Inferring interannual changes in global upper ocean heat storage from TOPEX altimetry. *Journal of Geophysical Research – Oceans* 100, 24943–24954.
- Willis, J.K., Roemmich, D., Cornuelle, B., 2003. Combining altimetric height with broadscale profile data to estimate steric height, heat storage, subsurface temperature, and sea-surface temperature variability. *Journal of Geophysical Research – Oceans* 108, C9, 3292.
- Willis, J.K., Roemmich, D., Cornuelle, B., 2004. Interannual variability in upper ocean heat content, temperature, and thermosteric expansion on global scales. *Journal of Geophysical Research – Oceans* 109, C12036.
- Willis, J.K., Lyman, J.M., Johnson, G.C., Gilson, J., 2009. In situ data biases and recent ocean heat content variability. *Journal of Atmospheric and Oceanic Technology* 26, 846–852.
- Wu, C.C., Lee, C.Y., Lin, I.I., 2007. The effect of the ocean eddy on tropical cyclone intensity. *Journal of the Atmospheric Sciences* 64, 3562–3578.
- Yasuda, I., Okuda, K., Hirai, M., 1992. Evolution of a Kuroshio warm-core ring – variability of the hydrographic structure. *Deep-Sea Research* 39, 131–161.